



The self-assembly and formation mechanism of regenerated cellulose films for photocatalytic degradation of C.I. Reactive Blue 19

Ji Fan · Dan Yu · Wei Wang · Baojiang Liu

Received: 9 November 2018 / Accepted: 26 February 2019 / Published online: 5 March 2019
© Springer Nature B.V. 2019

Abstract In this paper, a simple method has been developed to fabricate flexible fiber materials with excellent visible light response. Firstly, polydopamine (PDA) layer was deposited on the cotton fibers to functionize cotton fibers. Then, a uniformly dense layer of silver and tungsten trioxide nanoparticles was obtained on cotton fabric by reduction of PDA. The deposition of PDA provided a media for the Ag–WO₃ photocatalyst to be loaded with good adhesion. The results showed that the prepared cotton (C)-PDA–Ag–WO₃(c) composite photocatalytic material exhibited excellent photocatalytic performance with 98% degradation efficiency of RB-19 dye solution within 180 min under visible light irradiation. Moreover, the degradation rate constants were 52.43 ×, 35.73 ×, 12.01 × and 3.77 × higher than those of raw cotton, C-PDA, C-PDA-Ag and C-PDA-Ag–WO₃(a), respectively. The free radical trapping experiments showed that h⁺, ·OH and ·O₂[−] were important active species in the photocatalytic process. Based on the characterizations of the system, the possible photocatalytic

reaction mechanism of the C-PDA-Ag–WO₃(c) composite photocatalytic material was proposed. This paper provided a new perspective for the preparation of high catalytic performance visible light responsive flexible fiber materials applied in the degradation of dye wastewater.

Keywords C-PDA-Ag–WO₃(c) · Photocatalytic fabric · Photodegradation · Visible light · Recycle and reuse

Introduction

In the past few decades, the harm of environmental pollution to human health has attracted great attention as they (especially wastewater pollution) have become a major threat to human survival and safety. In order to solve the problem of wastewater pollution, many technologies have been developed (such as adsorption, filtration, extraction, membrane separation, Fenton-reagent method and photocatalysis technology). Among them, photocatalysis has been widely used in water pollution treatment due to its economical, high efficiency and environmental friendly (Maeda 2011; Liu et al. 2018; Zhu et al. 2017). Obviously, the development of photocatalytic technology is to fabricate photocatalysts with excellent performance and recyclability. At present, many types of semiconductor photocatalytic materials have been developed into

J. Fan · D. Yu · W. Wang · B. Liu (✉)
College of Chemistry, Chemical Engineering and
Biotechnology, Donghua University, Shanghai 201620,
China
e-mail: bjliu@dhu.edu.cn

J. Fan · D. Yu · W. Wang · B. Liu
Zhejiang Province New Textile Research and
Development Emphasised Laboratory, Hangzhou 310009,
China

photocatalytic materials such as metal oxides (TiO_2 , ZnO , WO_3), metal sulfides (Ag_2S , ZnS), metal nitrides (Ta_3N_5) and the like (Antoniadou et al. 2011; Higashi et al. 2011; Shuang et al. 2018; Wenderich and Mul 2016; Zhu et al. 2018; Wang et al. 2018b; Ji et al. 2018). However, most photocatalytic materials cannot absorb visible light energy, which greatly restricts their application scope. In recent years, noble metal photocatalysts have attracted extensive attention from researchers due to their ability to inhibit the combination of photogenerated electrons and holes, such as Au/TiO_2 , Ag/AgBr and $\text{Ag}_3\text{PO}_4/\text{Ag/WO}_3$ (Bu et al. 2015; Panayotov et al. 2017; Xie et al. 2015). Among them, the surface plasmon resonance (SPR) of noble metal Ag can not only absorb visible light intensively, but also conduct photo-generated electrons effectively. This founding greatly improves the photocatalytic efficiency and ensures a broad application prospect.

Currently, semiconductor photocatalysts are generally fabricated into three shapes. The first one is a powder-shaped semiconductor nanophotocatalytic material, including nanoparticles, nanosheets, nanorods, nanotubes and so on (Elmaleh et al. 2008; Hu et al. 2012; Lv et al. 2017; Yu et al. 2009). These nanopowders generally exhibit excellent photocatalytic properties due to their nanoparticles and large specific surface area, but are easily lost in degrading process. The second one is to grow semiconductor nanofilms on flat substrates such as ITO glass or metal foil (Limmer et al. 2004; Tian et al. 2012). Although these film-like photocatalysts are recyclable and can be effectively recycled, they still have some disadvantages such as high-cost, low flexibility and specific surface area. The last one is to fabricate semiconductor nanofibers (TiO_2/ZnO and Bi_2O_3) (Boyadjiev et al. 2017; Wang et al. 2009) and nonwoven fabrics by electrospinning (such as $\text{Ta}_3\text{N}_5\text{-Pt}$ (Li et al. 2014) and $\text{Fe}_2\text{O}_3\text{-AgBr}$ (Zhao et al. 2015)). However, these prepared semiconductor nanofibers and nonwoven fabrics have poor mechanical properties, particularly used in flowing waste water. Therefore, it is necessary to develop a new photocatalyst with good mechanical strength, excellent flexibility, low cost and high catalytic activity to degrade environmental sewage.

Dopamine (DA) is a kind of catecholamines with good biocompatibility, which can generate polydopamine (PDA) by self-polymerization and formed an adhesive coating on various materials, which was

inspired by the characteristics of viscous proteins in mussels (Gao et al. 2013; Schlaich et al. 2018). PDA possesses functional groups in its chemical structure like catechol, amines and imines, which can be used as a starting point for covalent modification with a desired molecule, or as an anchor point for the loading transition metal ions, and a plurality of hybrid materials can be further produced by the strong reducing ability of these metal ions under alkaline conditions (Liu et al. 2014; Pan et al. 2018; Zhang et al. 2017a). Therefore, Ag nanoparticles can be produced by PDA reduction, and then a visible-responsive silver-based photocatalyst was fabricated.

To obtain robust photocatalysis performance, we consider to use tungsten trioxide (WO_3), which belongs to n-type semiconductor material with band gap between 2.5–3.5 eV and belongs to a class of wide band gap oxides. As a kind of semiconductor material with development potential, it has broad application prospects in gas sensor, photocatalysis, photoelectrocatalysis and monitor (Cheng et al. 2018; Naik et al. 2013; Paz et al. 2018; Wang et al. 2016, 2017b; Zhang et al. 2016a). In addition, WO_3 is a very stable metal compound under acidic conditions. It also has some characteristics, including medium hole diffusion length (~ 150 nm) and high oxidation potential of valence band (VB) holes (about + 3.49 eV vs SHE) (Hu et al. 2018; Wang et al. 2017a; Yu et al. 2017). These advantages indicate that it may generate charge transitions in the visible light range. It should be pointed out that both crystalline WO_3 ($\text{WO}_3(\text{c})$) and amorphous WO_3 ($\text{WO}_3(\text{a})$) have high oxidation potential of VB holes. However, $\text{WO}_3(\text{c})$ has higher photocatalytic activity than $\text{WO}_3(\text{a})$, because $\text{WO}_3(\text{c})$ nanoparticles possessed much more amounts of coordination unsaturated W sites (Li et al. 2019). Owing to this unsaturated coordination environment, the $\text{WO}_3(\text{c})$ exhibited a higher photocatalytic activity in the degradation of RB-19. Nevertheless, the original WO_3 tends to exhibit lower photocatalytic efficiency due to its low solar energy absorption, high photo-generated electron hole recombination rate and its low conduction band (CB) position, which greatly limits the improvement of photocatalytic activity. Fortunately, in order to enhance the photocatalytic activity of WO_3 , some strategies have been adopted including morphology and dimension controlling, surface sensitization, addition of metallic and non-metallic dopants and the construction of nanocomposites so

as to improve the photocatalytic activity of semiconductor photocatalysts (Momeni and Ghayeb 2015; Momeni et al. 2015; Vallejos et al. 2011). In particular, doping with different noble or non-noble metal nanoparticles (such as Pt, Au, Cu, Zn, etc.) was considered to be an excellent method for improving the light absorbing ability and photoelectrocatalytic activity of WO_3 . Gan et al. used a new and simple method to directly fabricate 3D flower-like WO_3 , and silver nanoparticles were then deposited on the surface of WO_3 by a method of in situ redox reaction. The results show that the as-prepared Ag@WO_3 plasma photocatalyst has a good photocatalytic performance (Zhang et al. 2018). Xi et al. used a general in situ reaction between weakly reducing carbonaceous microspheres and an oxidizing noble metal precursor to synthesize a uniform Au-WO_3 porous hollow sphere on a large scale without other reducing agents and stabilizing agents. And it proved that this material has excellent activity for photocatalytic degradation of organic pollutants (He et al. 2017). Liu et al. (2018) prepared a novel Ag/AgCl/WO_3 plasmonic Z-scheme photocatalyst by a simple method. As a result, it was found that the photocatalyst exhibited excellent photocatalytic properties. Although some photocatalysts for WO_3 doped noble metal nanoparticles have been studied, such photocatalysts still have disadvantages such as difficulty in recovery and easy loss. In addition, these photocatalysts are not only easy to cause secondary pollution, but also has high treatment cost and unsuitable for large-flow wastewater treatment (Chen et al. 2019; Dong et al. 2019; Zhou et al. 2019). At the same time, the priority removal of toxic target pollutants in the presence of a large amount of organic/inorganic compounds is also quite difficult. Hence, it is extremely necessary to develop an effective photocatalytic system with excellent photocatalytic performance, multiple cycles of recycling and no secondary pollution to meet practical applications.

Based on the above discussion, the biggest challenge in the practical application of photocatalyst is how to solve some problems such as recovery and reuse of photocatalyst. Some researchers have suggested that photocatalysts should be fixed on some substrates (such as fabrics, fibers or glass). (Al-Ghafri et al. 2018; Han et al. 2012; Hu et al. 2017; Wang et al. 2018a). Among these proposed substrates, textiles have proven to be the best materials for supporting

photocatalysts due to their abundant porous structure, large specific surface area and wide range of sources. It is well known that cotton fabrics are one of the most popular materials with excellent flexibility and a special loose and porous structure (Hu et al. 2010b). These advantages can promote better absorption of dye molecules by cotton fabrics and easier recovery and recycling of the photocatalysts. Our group has once reported a cotton-based flexible cotton/polydopamine/ Ag/AgCl composite photocatalyst (Ding et al. 2018), but the preparation of this photocatalyst was costly and the preparation process was lengthy. In order to further study and design fiber-based composite photocatalytic materials, we proposed a new green method to prepare photocatalysts with excellent visible light response.

In this paper, a novel method for preparing a stable fiber-based PDA- $\text{Ag-WO}_3(\text{c})$ composite photocatalytic material by using polymerization crosslinking of DA, reduction of PDA, and oxidation of hydrogen peroxide. The prepared C-PDA- $\text{Ag-WO}_3(\text{c})$ composite photocatalytic material exhibits excellent flexibility, recyclability, strong visible-light absorption and high photocatalytic properties for degrading RB-19 dye solution. In addition, the mechanism of photocatalytic degradation of dye wastewater was further studied by using free radical and holes trapping experiments, which laid a solid foundation for better understanding of photocatalysis.

Experimental

Reagents and materials

In this experiment, 120 g m^{-2} plain cotton fabric (Esquel Group, China) was used. The cotton fabric was ultrasonically washed with deionized water and absolute ethanol prior to use. Reactive dyes (RB-19) were obtained from Dystar Printing and Dyeing Technology Co., Ltd. Tungsten hexachloride (WCl_6 , 99.5%) was purchased from Sinopharm Chemical Reagent Co., Ltd. Sodium oxalate (Na-OA) with 99% purity, 2-methyl-2-propanol (t-BuOH) with 99% purity, and 1,4-p-benzoquinone (BQ) with 99% purity were all purchased from Adamas Reagent Co., Ltd. Silver nitrate (AgNO_3) and dopamine hydrochloride (DA) with 99% purity were purchased from Shanghai Chemical Reagent Co., Ltd. Other chemicals used in

the test were obtained from Sinopharm Chemical Reagent Co., Ltd. All chemicals were of analytical grade, and used without further purification.

Preparation of visible light responsive flexible composite photocatalytic fabric

A schematic diagram of the preparation process of the visible light responsive composite photocatalytic fabric was shown in Fig. 1.

Preparation of C-PDA composite photocatalytic fabric

Firstly, 0.4 g of DA was dissolved in 200 mL deionized water to prepare a DA solution with a concentration of 0.01 mol/L. And the pH value of this solution was adjusted to 8.5 by 1 mol/L NaOH solution. Secondly, the washed cotton fabric was dipped into the freshly prepared DA solution and stirred at 30 °C for 24 h. After the reaction was completed, the fabric was removed and thoroughly washed with deionized water to remove possible impurities. Finally, the fabric was dried in an oven at 50 °C. In the subsequent discussion, the cotton fabric

treated by DA solution will be referred to as C-PDA (short for Cotton-Dopamine fabric).

Preparation of C-PDA-Ag composite photocatalytic fabric

0.2 g of AgNO_3 was first dissolved in 200 mL deionized water to prepare AgNO_3 solution with the concentration of 5.90 mol/L, and then the as-prepared C-PDA was immersed in the AgNO_3 solution and stirred at 30 °C for 3 h. Thereafter, the sample was washed with deionized water for 5 min and dried for 3 h in an oven at 60 °C. The final sample was referred as C-PDA-Ag (short for Cotton-Dopamine-Ag fabric).

Preparation of C-PDA-Ag- $\text{WO}_3(\text{a})$ composite photocatalytic fabric

WCl_6 solution with 0.25 mol/L concentration was prepared by dissolving 2.0 g WCl_6 in 20 ml of absolute ethanol. Thereafter, the as-prepared C-PDA-Ag was immersed in WCl_6 solution for 10 min at 30 °C. The sample was then taken out and dried for 3 h in an oven at 60 °C. Finally, the prepared fabric was subjected to UV irradiation for 10 min to remove Cl^- remaining in the fabric (Cheng et al.

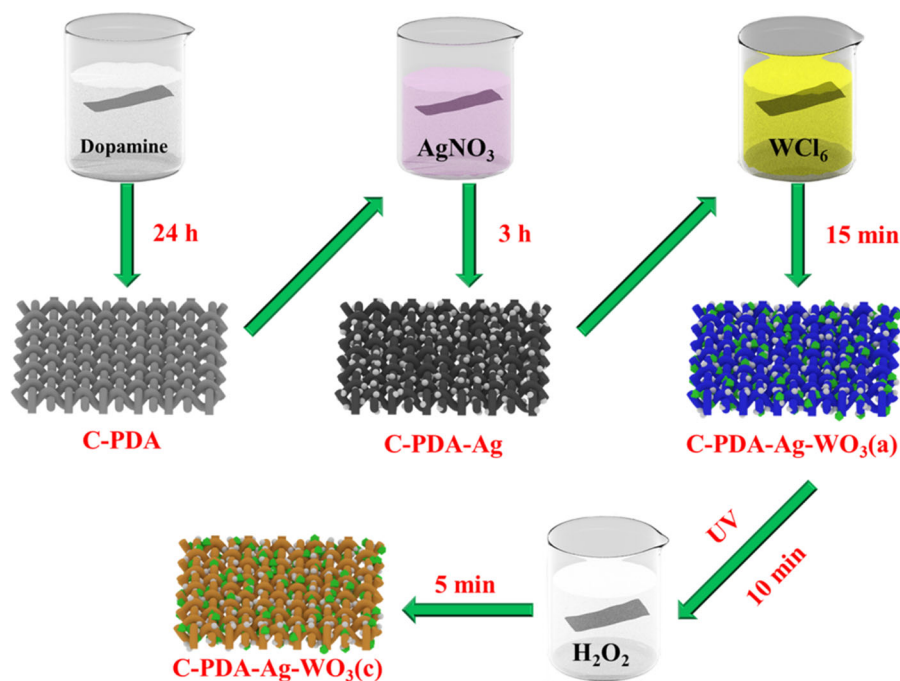


Fig. 1 Preparation of C-PDA-Ag- $\text{WO}_3(\text{c})$ composite photocatalytic fabric

2018). In the following discussion, this sample will be called as C-PDA-Ag-WO₃(a) (short for Cotton-Dopamine-Ag-WO₃(amorphous) fabric).

Preparation of C-PDA-Ag-WO₃(c) composite photocatalytic fabric

After irradiation, the as-prepared C-PDA-Ag-WO₃(-a) was placed in 50 ml of deionized water and dripped with two drops of hydrogen peroxide. After the samples were completely oxidized to yellow, it was taken out and dried for 3 h in an oven at 60 °C. In the following discussion, this sample will be called as C-PDA-Ag-WO₃(c) (short for Cotton-Dopamine-Ag-WO₃(crystalline) fabric).

Characterization

The morphology of the composite photocatalytic fabric was observed by field emission scanning electron microscopy (FE-SEM) with model S4800. The element content and distribution of the prepared samples were observed by energy dispersive spectrometer (EDS). X-ray photoelectron spectroscopy (XPS) was used to measure and record the chemical oxidation state of the composite photocatalytic fabric. The UV-vis diffuse reflectance spectra (UV-vis DRS) of the samples were determined by a spectrophotometer of type UV-3600.

Photoelectrochemical measurement

The photoluminescence (PL) properties were measured on a PTI QM/TM fluorescence spectrometer with the excitation at 325 nm. The photocurrents and electrochemical impedance spectroscopy (EIS) measurements were performed on an electrochemical analyzer (model PGSTAT302 N) in which the counter electrode and the reference electrode were Pt flake and Ag/AgCl, respectively.

Refining and purification for RB-19 dye

Firstly, 10 g of the RB-19 dye was dissolved in 40 ml of N,N-dimethylformamide, followed by filtration to remove impurities in the filtrate. Thereafter, 100 ml of

acetone solution was added to the filtrate to precipitate a dye, which was allowed to place at room temperature for 12 h. Finally, the refined and purified dye was filtered and dried in a vacuum oven at 50 °C for 3 h.

Photocatalytic performance evaluation

In this experiment, we used a photochemical reactor to determine the photocatalytic effect of the composite photocatalytic fabric. The photocatalytic performance of C-PDA-Ag-WO₃(c) composite photocatalytic fabric (size 5 × 5 cm²) was evaluated by observing the photocatalytic degradation of RB-19 dye under visible light irradiation. In the whole process, visible light irradiation was simulated by using a 1000 W Xe lamp radiant tube equipped with a 400 nm cut-off filter to remove UV light at ambient temperature. During the reaction, the cooling water circulator was always turned on to keep the entire reaction system at a constant temperature. Typically, the prepared C-PDA-Ag-WO₃(c) composite photocatalytic fabric was placed in quartz tubes containing 50 mL RB-19 dye solution at a concentration of 50 mg/L. Thereafter, maintain continuous agitation of the entire system to ensure uniformity of the dye solution. Before starting the photoreaction, the quartz tube was first stirred under dark conditions for 30 min to reach the adsorption-desorption dynamic equilibrium, and then the photochemical reactor was turned on to start the photocatalytic degradation reaction. During the reaction, about 5 ml of the degradation solution was taken out every 30 min and its absorbance was measured at a specific wavelength (590 nm) using an ultraviolet-visible spectrophotometer (model U3310).

In addition, in order to investigate the photocatalytic stability and reusability of the C-PDA-Ag-WO₃(c) composite photocatalytic fabric, five consecutive photocatalytic cycle tests were measured under visible light irradiation. After each cycle, the C-PDA-Ag-WO₃(c) sample was thoroughly washed with deionized water and dried at 60 °C for 3 h, then placed in a quartz tube containing 50 ml of RB-19 dye solution at a concentration of 50 mg/L. More importantly, a possible photocatalytic reaction mechanism was proposed by investigating the photocatalytic degradation of RB-19 dye solution with various scavengers.

Results and discussion

The possible reaction mechanism of dopamine and various chemical reagents

This paper proposed a possible reaction mechanism between dopamine and different chemical reagents, and the specific flow diagram was shown in Fig. 2.

First, DA (3,4-dihydroxyphenethylamine) can undergo self-polymerization and cross-linking under mild conditions to generate PDA. The catechol group of the formed PDA film was chelated with Ag^+ and then the Ag^+ was reduced to Ag nanoparticles in situ. At this time, the catechol groups were simultaneously oxidized into quinone structures (Long et al. 2011; Wang et al. 2013; Xu et al. 2011). Finally, $\text{Ag}@\text{WO}_3$ composite nanoparticles were formed by impregnating the WCl_6 solution and subjecting it to UV light, followed by oxidation of the product with hydrogen peroxide. It should be pointed out that the self-polymerization and cross-linking mechanism of DA and the interaction mechanism between PDA and substrate have not been fully studied so far.

Characterization of the as-prepared composite photocatalytic fabric

XRD analysis of the as-prepared composite photocatalytic materials

X-ray powder diffraction analysis was performed to study the crystal structures of pure and doped samples and Fig. 3 showed the typical XRD patterns of the prepared composite photocatalytic fabrics. It can be seen from Fig. 3a that the apparent diffraction peaks of C-PDA-Ag- WO_3 (a) and C-PDA-Ag- WO_3 (c) composite photocatalytic materials at 26.59° and 34.16° belong to the monoclinic phase of WO_3 (JCPDS No. 43-1035) (120) plane and (202) plane (Sun et al. 2017). This indicates that the loading of WO_3 did not affect the crystal phase structure of the C-PDA-Ag composite material. In addition, it can be observed that C-PDA-Ag, C-PDA-Ag- WO_3 (a) and C-PDA-Ag- WO_3 (c) composite photocatalytic materials exhibited diffraction peaks at $2\theta = 38.89^\circ$ and 46.04° . These two diffraction peaks correspond to the (310) and (312) plane of Ag (JCPDS No. 65-2871) (Dong et al. 2013). Figure 3b is a partial amplification XRD image of C-PDA-Ag, C-PDA-Ag- WO_3 (a) and C-PDA-Ag- WO_3 (c) composite photocatalytic fabrics. However, no impurities of other characteristic peaks such as the presence of Ag_2CO_3 or Ag_2O were detected. This demonstrated that the prepared photocatalytic fabrics are mainly consisted of Ag and WO_3 .

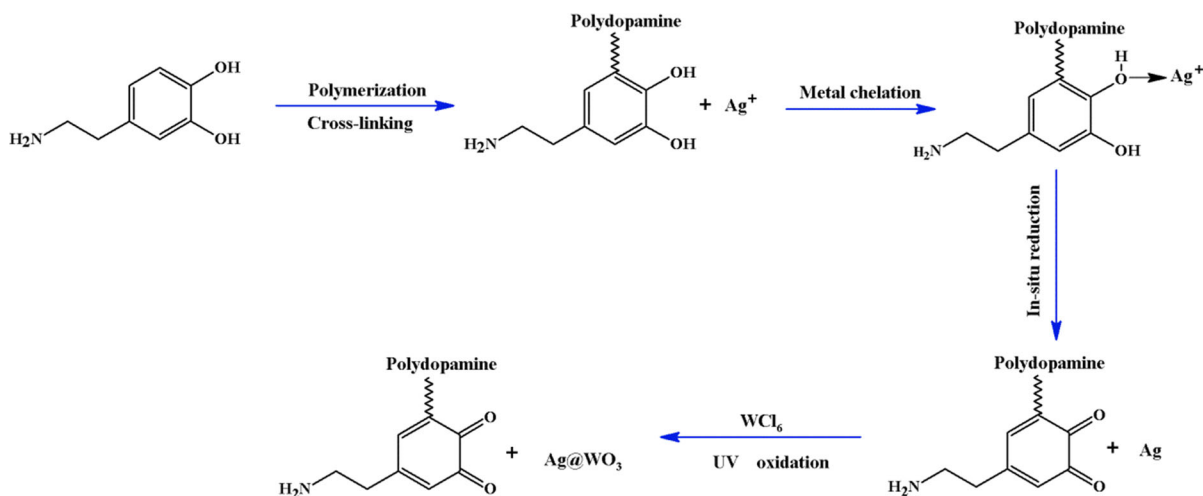


Fig. 2 Proposed a possible interaction mechanism for dopamine and different chemical reagents

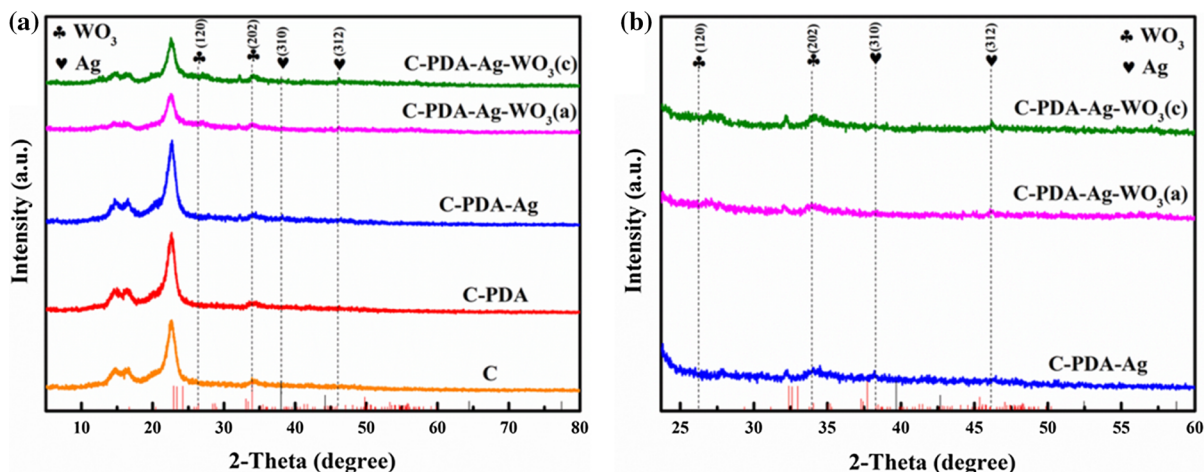


Fig. 3 **a** XRD patterns of C, C-PDA, C-PDA-Ag, C-PDA-Ag-WO₃(a) and C-PDA-Ag-WO₃(c); **b** partially amplified XRD patterns of C-PDA-Ag, C-PDA-Ag-WO₃(a) and C-PDA-Ag-WO₃(c)

FE-SEM analysis of the as-prepared composite photocatalytic materials

The surface morphology and local structure of the as-prepared composite photocatalytic fabrics were observed by FE-SEM. In Fig. 4a, b, it can be observed that the raw cotton fabric surface was smooth and there are no obvious impurities on the fiber surface. However, after the cotton fabric was oxidatively polymerized with dopamine, it can be easily found from Fig. 4c, d that the surface of the raw cotton fabric was covered with a uniform film. At this point, PDA formed a support on the surface of the raw cotton fabric, and the change in the surface morphology of the C-PDA sample further confirmed the successful deposition of PDA on the raw cotton fabric.

The image of C-PDA-Ag [Fig. 4e, f] sample showed that Ag nanoparticles with uniform distribution have been successfully prepared on the surface of C-PDA sample by directly reducing Ag⁺ with PDA at room temperature using PDA as a carrier. Moreover, the magnified image of Fig. 4f clearly showed the regular three-dimensional structure of Ag nanoparticles with a size of about 40 nm. When the C-PDA-Ag sample was immersed in WCl₆ solution and treated by H₂O₂ oxidation, the stereostructure of WO₃ nanoparticles with a size of about 80 nm could be observed on the surface of the as-prepared C-PDA-Ag-WO₃ (a) [Fig. 4g, h] and C-PDA-Ag-WO₃(c) [Fig. 4i, j] composite photocatalytic fabrics, indicating that WO₃ had been successfully loaded on the fabrics. This further confirms the XRD analysis described above,

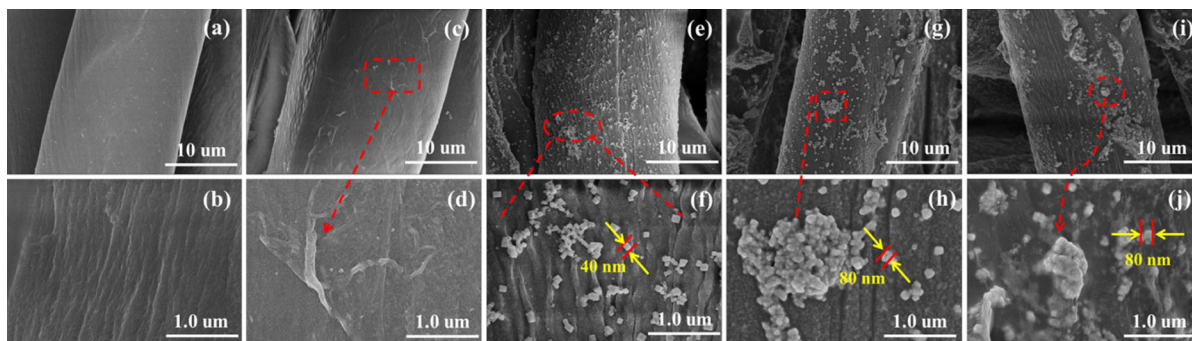


Fig. 4 FE-SEM images of raw cotton sample (a–b), C-PDA sample (c–d), C-PDA-Ag sample (e–f), C-PDA-Ag-WO₃(a) sample (g–h) and C-PDA-Ag-WO₃(c) sample (i–j)

which will also be demonstrated by subsequent EDS-mapping measurements.

EDS-mapping analysis of the as-prepared composite photocatalytic materials

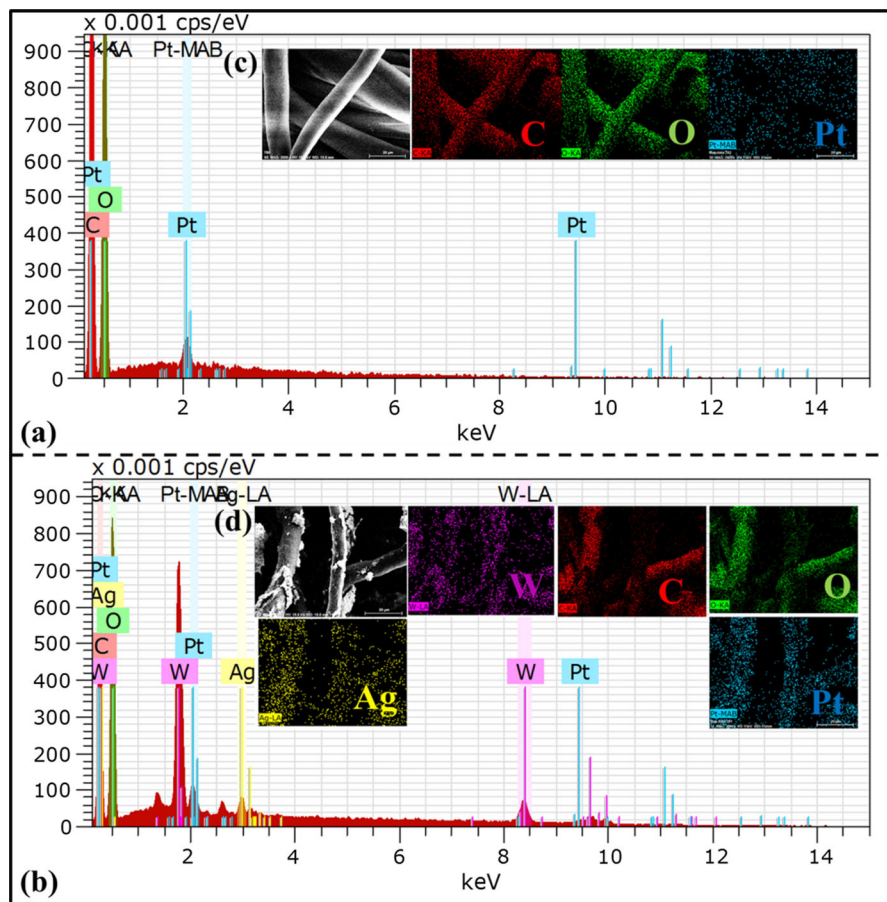
Subsequently, the composition of C-PDA and C-PDA-Ag-WO₃(c) composite photocatalytic fabrics were investigated by EDS-mapping analysis. The EDS pattern showed that only C and O elements exist in the C-PDA composite fabric. The reason for the absence of N element was that cotton fabric contained only C and O elements, while the PDA film only covered the surface of the fabric [Fig. 5a]. However, the subsequent XPS analysis confirmed the presence of the N element, and the FE-SEM analysis described above also indicated that the PDA film was successfully formed and uniformly covered on the surface of the raw cotton fiber. In addition, the elemental mappings of the single fiber confirmed that the

elements C and O were also evenly dispersed in the fiber [Fig. 5c]. It can be seen from Fig. 5b that the W and Ag element signals were newly present in the C-PDA-Ag-WO₃(c) sample, wherein the W element and the Ag element come from the adding of WO₃ and Ag element. And the elemental mapping results revealed that the elements of C, O, Ag and W were homogeneously distributed in the entire fiber [Fig. 5d]. It should be noted that the uniform distribution of the Ag and W elements proves that the existence of PDA film is beneficial for the even dispersion of the WO₃ and Ag nanoparticles. The above FE-SEM analysis also supported this conclusion from the side.

XPS analysis of the as-prepared composite photocatalytic materials

The chemical oxidation state of C-PDA-Ag-WO₃(c) composite photocatalytic fabric was investigated

Fig. 5 EDS-mapping analysis of C-PDA sample (a and c) and C-PDA-Ag-WO₃(c) sample (b and d)



by XPS. A wide scanning XPS spectrum of the composite photocatalytic material can be clearly observed from Fig. 6a. At the same time, the absorption peaks of five elements of W, O, N, Ag and C were presented, which was in agreement with the result of the above EDS analysis. In addition, Fig. 6b–f showed the high-resolution XPS of W 4f, Ag 3d, C 1s, N 1s and O 1s of C-PDA-Ag-WO₃(c) composite photocatalytic fabric, respectively. Figure 6b revealed the XPS spectrum of W 4f, which can be deconvoluted into four peaks in the range of 31–40 eV. Two main peaks emerged at 36.31 and 34.21 eV were related to W 4f_{5/2} and W 4f_{7/2} of the W⁶⁺ atoms, while the peaks at 37.07 and 34.66 eV were well combined with the W⁵⁺ atoms (Cao et al. 2018; Ding et al. 2017; Meng et al. 2015). These characterization results confirmed that the W element was mainly expressed in two states of W⁶⁺ and W⁵⁺ (Zhang et al. 2017a), suggesting the existence of oxygen vacancies in WO₃ (Shirke and Mukherjee 2017). The absorption peaks appearing at 372.08 eV and 366.02 eV were confirmed to be consistent with Ag 3d_{3/2} and Ag 3d_{5/2} of metallic Ag, and the specific results were shown in the Fig. 6c (Ramstedt and Franklyn 2010). The formation of Ag⁰ can be assigned to photochemical reduction of PDA, which further demonstrated the existence of Ag

nanoparticles in the C-PDA-Ag-WO₃(c) composite photocatalytic fabric. Figure 6d exhibited the deconvolution result of C 1s. Four peaks, located at 283.13 eV, 284.71 eV, 285.22 eV and 286.31 eV, correspond to C–C, C–N, C–O and C=O, respectively (Zhang et al. 2013). The N 1s spectrum can be decomposed into two peaks, where the peaks of 398.49 and 399.38 eV were distributed to =N–R and R–NH–R, and the results were shown in Fig. 6e. It is worth noting that the appearance of element N was mainly attributed to the introduction of PDA. The R–NH–R bond was derived from the amine functional group of DA, while the =N–R bond was assigned to the indole group (formed by DA oxidation self-polymerization) (Yin and Liu 2008). Furthermore, the XPS spectrum of O 1s could be divided into five distinct absorption peaks, the peaks at binding energies of 532.19, 531.81, 531.32, 530.67, 529.49 and 528.82 eV should be classified as O=C, O=C–O, C–O, W–OH, O=W and O–W bonds, respectively (Ding et al. 2016; Zhang et al. 2017b).

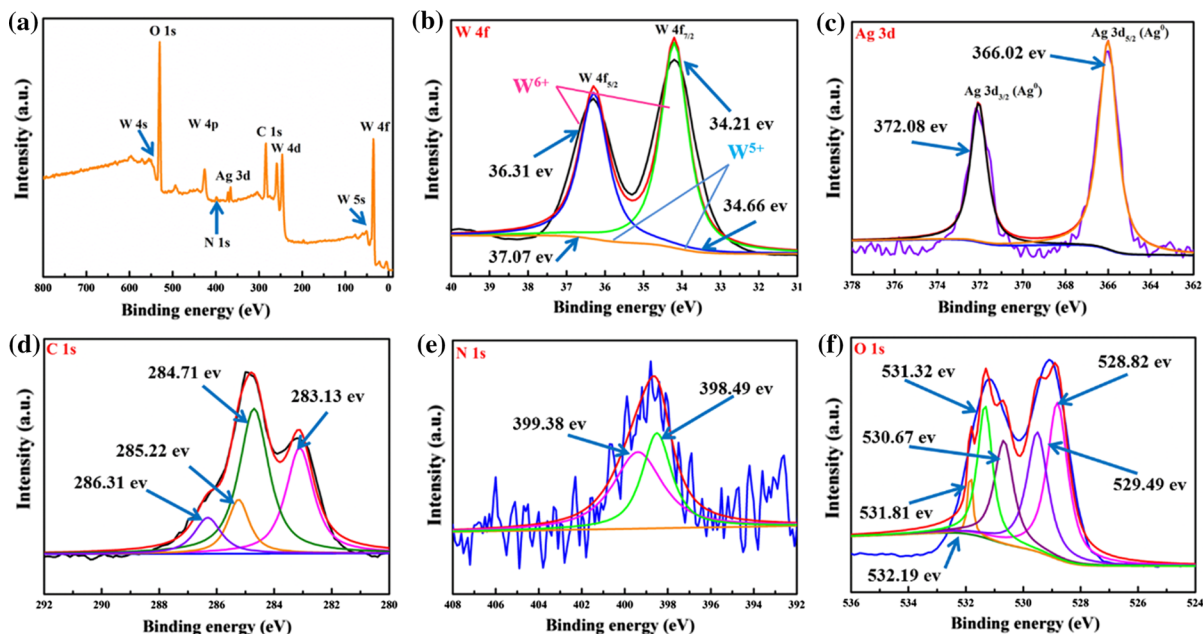


Fig. 6 XPS wide-scan spectra (a) and its high-resolution XPS spectra of W 4f (b), Ag 3d (c), C 1s (d), N 1s (e) and O 1s (f) of C-PDA-Ag-WO₃(c) sample

UV–vis diffuse reflectance analysis of the as-prepared composite photocatalytic fabric

The light absorption properties of prepared composite photocatalytic fabrics were investigated by UV–vis diffuse reflectance spectroscopy (UV–vis DRS). As can be clearly seen from the Fig. 7a, the untreated cotton fabric has no significant absorption in the UV–vis region. Compared with raw cotton fabric without absorbance at all, C-PDA photocatalytic fabric shows absorption in the 200–800 nm regions, indicating that the PDA has the ability to absorb UV–visible light. Therefore, it can be obtained that the PDA can sufficiently absorb solar energy and stimulate the generation of electron–hole pairs, thereby promising to further enhance the photocatalytic performance. With the addition of metal Ag nanoparticles, C-PDA-Ag composite material exhibited stronger absorption in the UV–vis region. The appearance of this situation indicated that the SPR effect of metallic Ag nanoparticles exhibits effective plasmon resonance in the visible region, resulting in the generation of more electron–hole pairs (Varma et al. 2016). The C-PDA-Ag-WO₃(a) composite photocatalytic fabric absorbs widely in the UV–vis region and it has a significantly higher absorption intensity than the C-PDA-Ag sample. The main reason for this phenomenon is because WO₃ has the better visible light-induced photocatalytic properties and it can generate more electron–hole pairs after loading with Ag nanoparticles. Furthermore, due to the SPR effect of the metallic

Ag particles, the absorption intensity of Ag@WO₃ was significantly increased in the region of 500–800 nm (Sun et al. 2010). However, it can be found that the absorbance of the C-PDA-Ag-WO₃ (c) photocatalytic fabric in the UV light region of 200–380 nm was higher than that of the C-PDA-Ag-WO₃(a) sample, but the absorbance in the visible light region was reduced, which should be attributed to the decomposition of a part of the Ag nanoparticles by hydrogen peroxide during the oxidation process and the photocatalytic ability of WO₃ in the crystalline state to be higher than that of WO₃ in the metastable amorphous state. The above results indicated that the composite effect of C-PDA-Ag-WO₃ (c) composite photocatalytic fabric can strongly heighten the absorption of visible light, so as to make more effective use of solar energy.

Besides, the band structure of the semiconductor also plays a vital role in optical absorption characteristics. According to the UV–vis results obtained above, the band gap (E_g) of different photocatalytic fabrics were determined by the following equation:

$$(Ah\nu) = K(h\nu - E_g)^{n/2}$$

where A , h , ν , K and E_g represent the absorbance coefficient, Planck's constant (6.63×10^{-34} J s), frequency, a constant and the band gap energy, respectively. It should be noted that $\nu = c/\lambda$, c represents the speed of light (3.0×10^8 m/s) and λ represents the wavelength of light (Tauc 1966). And n refers to the characteristic value of the electronic transition in the

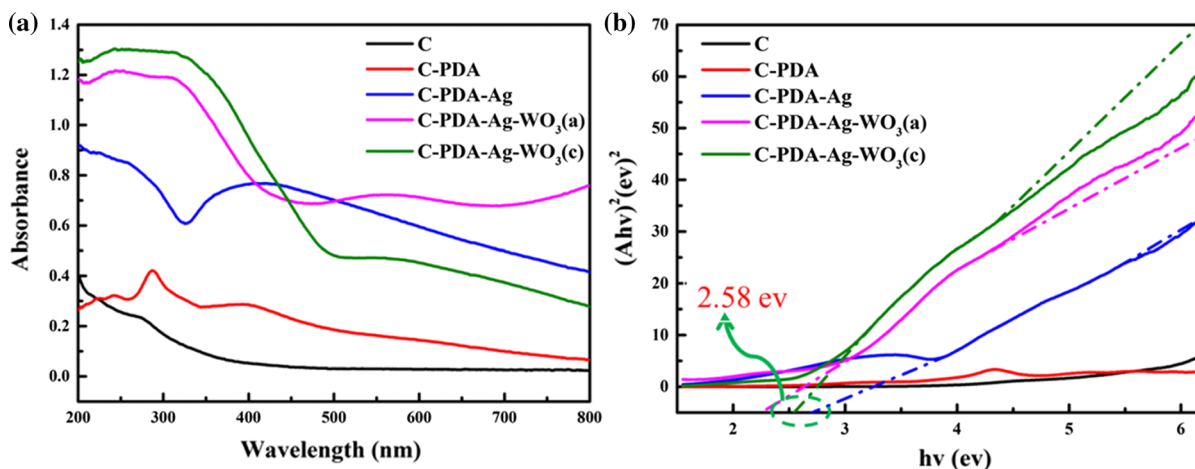


Fig. 7 **a** UV–vis diffuse reflectance spectra of all the samples and **b** band gap energy evaluation from the plots of $(Ah\nu)^2$ versus energy ($h\nu$) of the corresponding samples

semiconductor. For WO_3 , the value of n is 1. In Fig. 7b, the band gap energy of the as-prepared C-PDA-Ag- WO_3 (c) photocatalytic fabric was about 2.58 eV after calculation, which was in agreement with the reference value in literature (Li et al. 2018; Xie et al. 2015). However, the band gap energy of the C-PDA-Ag- WO_3 (a) composite photocatalytic fabric was calculated to be only 2.27 eV, which was significantly smaller than that of the C-PDA-Ag- WO_3 (c) composite photocatalytic fabric. Therefore, it can be concluded that the C-PDA-Ag- WO_3 (c) composite photocatalytic fabric has excellent photocatalytic effects.

Photoelectrocatalytic properties of the as-prepared composite photocatalytic fabrics

The kinetics of charge transfer in these composite photocatalytic fabrics was analyzed by EIS measurement and photocurrent response testing. Photoelectrode-electrolyte charge transfer resistance (CTR) is equivalent to the transmission and separation efficiency of photogenerated electron-hole pairs, which can be specifically represented by the arc diameter on Nyquist diagram (Shi et al. 2016). As can be seen from the Fig. 8a, the electrode arc-radius was much smaller for the C-PDA-Ag- WO_3 (c) compared with C-PDA, C-PDA-Ag and C-PDA-Ag- WO_3 (a), indicating that the CTR for C-PDA-Ag- WO_3 (c) composite photocatalytic material was decreased, which will accelerate charge migration and separation so as to reduce energy losses.

In order to further evaluate the photoelectrochemical activity of the composite photocatalytic fabric, the

transient photocurrent response was measured under the irradiation of 5 cycles of optical switch at 30 s interval. In general, the stronger the photocurrent intensity, the higher the separation and migration efficiency of e^- and h^+ in the photocatalytic reaction (Liang et al. 2015). As shown in Fig. 8b, the photocurrent density of C-PDA-Ag- WO_3 (c) was about $1.24 \mu\text{A cm}^{-2}$, which was much larger than C-PDA ($0.47 \mu\text{A cm}^{-2}$) and C-PDA-Ag ($0.26 \mu\text{A cm}^{-2}$) as well as C-PDA-Ag- WO_3 (a) ($0.94 \mu\text{A cm}^{-2}$). As expected, the value of C-PDA-Ag- WO_3 (c) was greater than the other samples, indicating that the C-PDA-Ag- WO_3 (c) has higher generation and migration efficiency for photo-generated electron-holes (Ma et al. 2017). These data adequately demonstrated that the as-prepared C-PDA-Ag- WO_3 (c) composite photocatalytic fabric can effectively promote the photogenerated charge migration and immediately reacted with the target so as to improve photocatalytic performance.

Also, PL emission spectrum was used to investigate the separation efficiency of photogenerated electrons and holes. Generally speaking, the lower PL intensity indicated that the probability of photogenerated holes and electrons recombination was small and the photoactivity was high. As presented in Fig. 8c, the luminescence intensity of C-PDA-Ag- WO_3 (c) was the lowest compared with other samples. This indicated that the formation of the Schottky barrier resulted in a lower photogenerated electron-hole pair recombination rate. The function of the Schottky barrier accelerated the separation and transfer of the photogenerated charges and it can produce excellent photocatalytic activity (Gondal et al. 2016; Yang et al. 2017b). According to the above conclusions, the

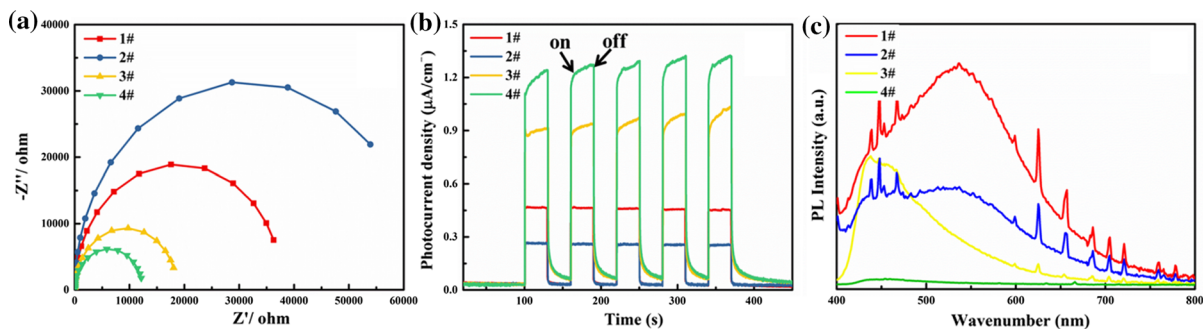


Fig. 8 a EIS profiles b Photocurrent response and c PL spectra for the different samples (where 1[#] stands for the C-PDA, 2[#] stands for the C-PDA-Ag, 3[#] stands for the C-PDA-Ag- WO_3 (a) and 4[#] represents to the C-PDA-Ag- WO_3 (c))

loading of Ag and WO_3 can help prevent the recombination of electrons and holes, and accelerate the effective separation of photogenerated electron holes and interface charge transfer. Hence, the C-PDA-Ag- WO_3 (c) photocatalytic fabric displayed higher photocatalytic properties. This also supported the analysis of the above UV-vis diffuse reflectance test from the side.

Adsorption and photocatalytic experiments of the as-prepared composite photocatalytic fabrics

The adsorption and photocatalytic activities of all prepared photocatalytic fabrics were estimated by the degradation of RB-19 dye solution and the results were shown in Fig. 9. Firstly, adsorption experiments were performed on all samples, in which the adsorption experiments were carried out under dark conditions. It can be seen from the Fig. 9a that the dye concentration in the tube was dropped to about 90% after 10 min of reaction. The reason for this phenomenon was that cellulose fibers have affinity for dye molecules, and the porous structure of the fiber was conducive to the adsorption of dye molecules. Then, it can be observed that the adsorption rate decreased slightly in the following 20 min and reached the equilibrium state of adsorption-desorption after 30 min. It should be pointed out that the strong affinity of the dye molecules to the cellulose fibers was an advantageous condition for enhancing the photocatalytic properties of the composite photocatalytic fabric.

To evaluate the photocatalytic properties of the different photocatalytic fabrics, the photodegradation ability of the obtained sample to the RB-19 dye solution was examined under visible light irradiation, and the results were presented in Fig. 9b. For all the samples, the decrease of the absorbance at 590 nm was used to monitor the degradation of the dye. For comparison, control experiment was also conducted under the same experimental conditions without photocatalytic fabric. As can be seen from the figure, the absorbance of dye residues degraded by different photocatalytic fabrics all decreased after 180 min of visible light irradiation. In particular, for C-PDA-Ag- WO_3 (c) sample, the maximum absorption peaks of RB-19 dye solution at 590 nm gradually diminished and almost disappeared for 180 min, indicating that

RB-19 dye solution was completely degraded by the C-PDA-Ag- WO_3 (c) composite photocatalytic fabric. In order to intuitively observe the degradation activity, the photographs of the corresponding material were shown in the inset of Fig. 9b. It can be seen that the C-PDA-Ag- WO_3 (c) sample had a better photocatalytic activity.

In Fig. 9c, the photocatalytic properties of the obtained photocatalytic fabric were estimated by degrading the RB-19 dye solution under visible light irradiation. As a control, the photocatalytic degradation experiments of raw cotton fabric and C-PDA fabric without photocatalyst loading were also measured. As indicated, after 180 min of irradiation, no obvious change in the concentration of the RB-19 dye solution was found, suggesting the fact that the raw cotton fabric and the C-PDA fabric did not have a photocatalytic degradation effect on the RB-19 dye solution. The reason for this phenomenon was that they only adsorb dye molecules without participating in the photocatalytic process. With C-PDA-Ag and C-PDA-Ag- WO_3 (a) as composite photocatalytic fabrics, the degradation efficiency of RB-19 dye solution reached approximately 40% and 70% after irradiation for the same time. Surprisingly, when C-PDA-Ag- WO_3 (c) sample was used, almost 98% of RB-19 dye solution was degraded after 180 min, indicating that this sample had excellent photocatalytic activity. The reason for this phenomenon mainly included the following two aspects. For one thing, due to the SPR effect of Ag nanoparticles, the loading of Ag made the photocatalytic fabric expressed stronger visible light activity. For another, the heterostructure formed between crystalline WO_3 and Ag caused the Ag nanoparticles to accelerate the photogenerated charge separation (Gondal et al. 2016; Zhang et al. 2018). Through this synergistic effect, C-PDA-Ag- WO_3 (c) samples displayed higher photocatalytic activity under visible light irradiation (Duan et al. 2017).

Furthermore, the photodegradation kinetics were investigated using an apparent first-order model ($\ln C_0/C_t = Kt$). It can be observed from the Fig. 9d that the corresponding $\ln C_0/C_t \sim t$ plot had a good linearity, confirming that the photocatalytic degradation of RB-19 dye solution obeyed the first-order kinetic role. It should be noted that K was a reaction rate constant and it can be acquired from the linearly correlated slope in the graph. The K_1 of the cotton fiber as a control test was 0.00030 min^{-1} , the K_2 of the C-PDA was

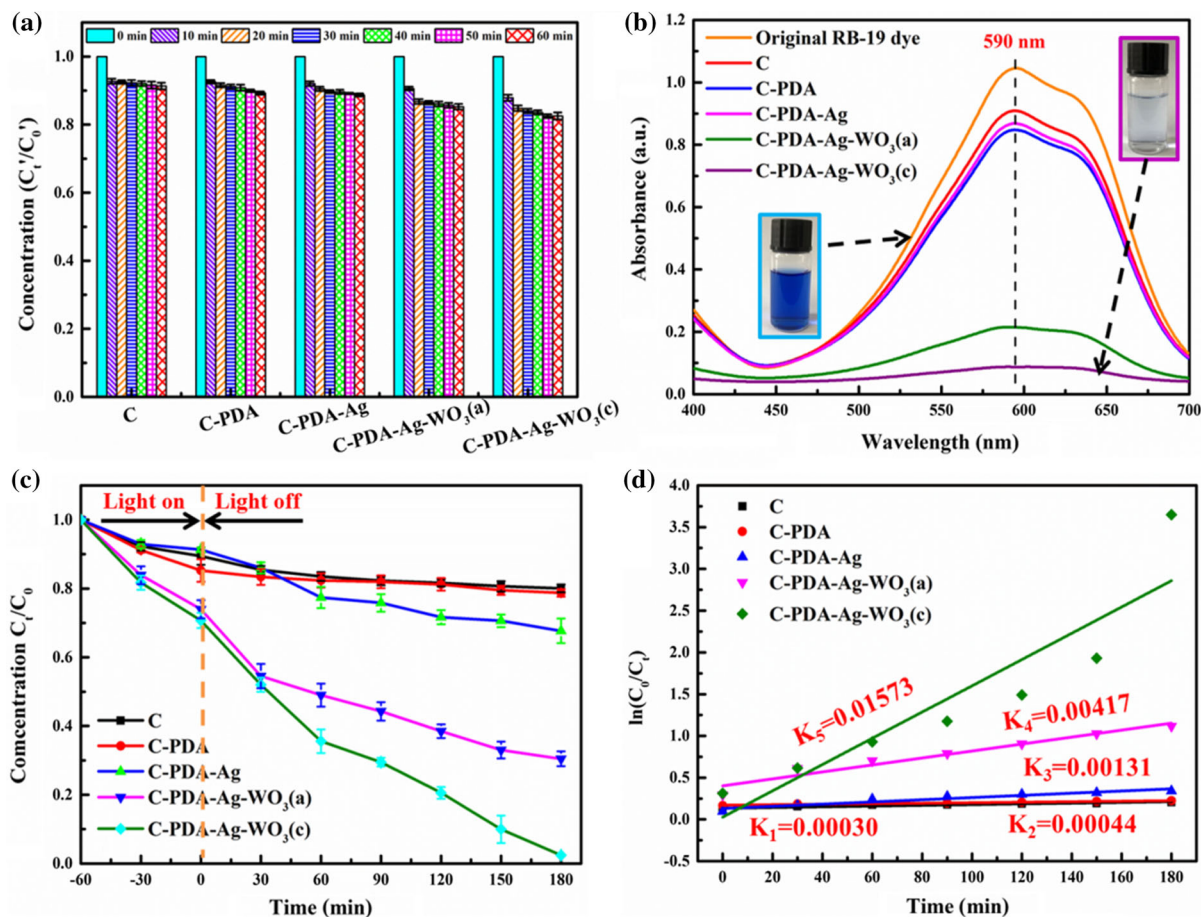


Fig. 9 **a** The adsorption–desorption equilibrium experiments of different photocatalytic fabrics within 60 min (where C_0' is the absorbance of RB-19 dye solution at initial concentration and C_t' is the absorbance of RB-19 dye solution at adsorption time t), **b** UV–visible absorption spectra of different samples irradiated for 180 min, **c** Photocatalytic degradation efficiency

of the RB-19 dye solution under visible light irradiation (where C_0 stands for the absorbance of adsorption equilibrium before irradiation experiment and C_t represents to the absorbance of RB-19 dye solution at irradiation time t) and **d** $\ln(C_0/C_t)$ against fitting curves for as-prepared different samples

0.00044 min^{-1} , the K_3 of the C-PDA-Ag was 0.00131 min^{-1} , and the K_4 of the C-PDA-Ag-WO₃(a) was 0.00417 min^{-1} . However, the K_5 of the C-PDA-Ag-WO₃(c) was 0.01573 min^{-1} . It was much higher than several other composite photocatalytic fabrics, which was consistent with the conclusions discussed previously.

Photocatalytic stability and reusability

The stability and reusability of the C-PDA-Ag-WO₃(c) are also not negligible in its practical applications. In this experiment, the C-PDA-Ag-

of the RB-19 dye solution under visible light irradiation (where C_0 stands for the absorbance of adsorption equilibrium before irradiation experiment and C_t represents to the absorbance of RB-19 dye solution at irradiation time t) and **d** $\ln(C_0/C_t)$ against fitting curves for as-prepared different samples

WO₃(c) photocatalytic fabric has a macroscopic size (area: $5 \times 5 \text{ cm}^2$) which can be easily taken out, washed, dried, and then reused. Herein, the stability of the C-PDA-Ag-WO₃(c) photocatalytic fabric was tested by four consecutive cycles (each cycle lasts 3 h) of degrading RB-19 dye solution under visible light irradiation under the same experimental conditions.

As shown in Fig. 10a, no significant deactivation was detected even after four consecutive runs (the photodegradation efficiency of RB-19 dye solution remains $\sim 85.2\%$), indicating that the obtained C-PDA-Ag-WO₃(c) photocatalytic fabric possesses excellent stability. In addition, the phase of the used

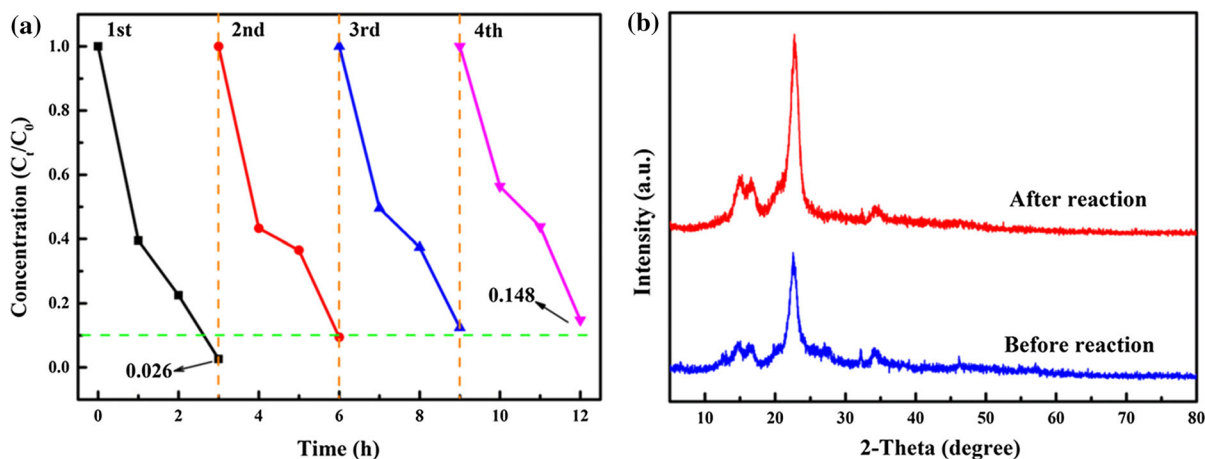


Fig. 10 **a** Cycling test in the photocatalytic degradation of RB-19 dye solution by C-PDA-Ag-WO₃(c) and **b** XRD pattern of C-PDA-Ag-WO₃(c) before and after a photocatalytic test

C-PDA-Ag-WO₃(c) photocatalytic fabric was further investigated. The XRD patterns [Fig. 10b] confirmed that there are no obvious changes in the crystalline phase of the C-PDA-Ag-WO₃(c) photocatalytic fabric before and after the recycling reactions. Thus, it can be concluded that the prepared C-PDA-Ag-WO₃(c) composite photocatalytic fabric has the ability to decompose organic contaminants rapidly and efficiently while having excellent stability and recyclability.

Mechanism of photocatalytic activity enhancement

The potential photocatalytic mechanism was further explored by free radical and hole scavenging experiments. In this paper, tert-butanol (t-BuOH) was used as $\cdot\text{OH}$ scavenger, sodium oxalate (Na-OA) as h^+ scavenger, and benzoquinone (BQ) was added as $\cdot\text{O}_2^-$ quencher (Dong et al. 2013; Hu et al. 2010a; Zhang et al. 2016b; Zhao et al. 2012). For comparison, a photocatalytic reaction without any scavenger was used as a blank test. Figure 11 exhibited the effect of these different scavengers on the degradation of RB-19 dye solution by C-PDA-Ag-WO₃(c) sample. The results showed that the degradation efficiency was significantly reduced from 97.8% to 30.9%, 27.9% and 14.5% after 180 min of the reaction using t-BuOH, Na-OA and BQ as the trapping agent compared to the no-scavenger under the same conditions. This means that these three trapping agents played a vital role in the photocatalytic reaction. Based on the above

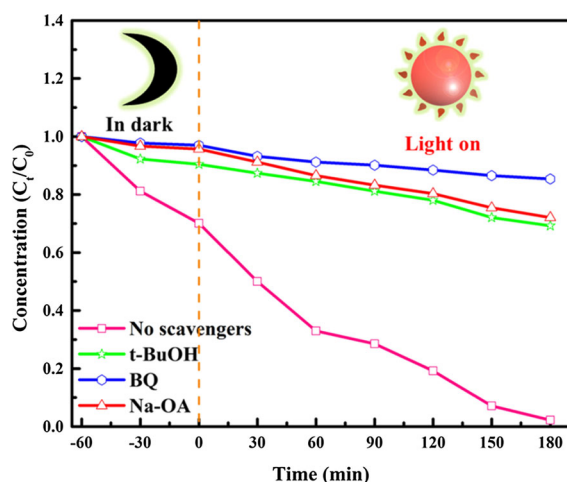
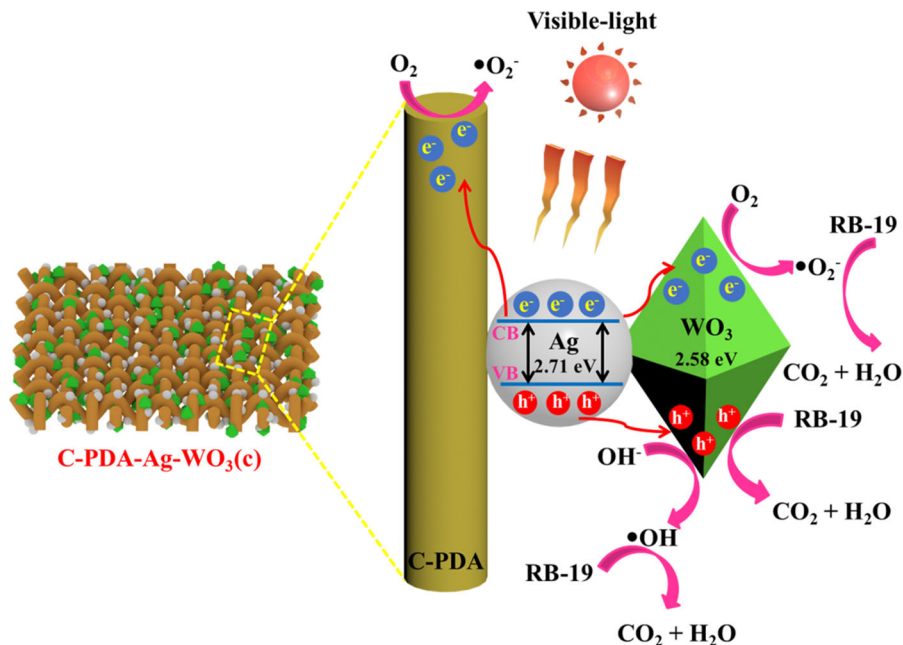


Fig. 11 Photocatalytic degradation performance of C-PDA-Ag-WO₃(c) sample for degrading the RB-19 dye solution in the absence or presence of various trapping agents: **a** no scavenger, **b** BQ, **c** Na-OA and **d** t-BuOH

results, it can be concluded that both h^+ , $\cdot\text{OH}$ and $\cdot\text{O}_2^-$ are the important active substances in the photocatalytic degradation process.

According to the above embodiments, the photocatalytic degradation mechanism of C-PDA-Ag-WO₃(c) composite photocatalytic fabric was proposed in Fig. 12. Generally speaking, cotton fabrics have a high specific surface area and a loose porous structure, which can absorb a large number of pollutants in a dark environment and reach the state of adsorption-desorption equilibrium. In addition, due to the conductivity of the PDA (Kim et al. 2014), the

Fig. 12 Schematic drawing of the experimental setup and the proposed photocatalytic degradation mechanism of C-PDA-Ag-WO₃(c) composites on RB-19 dye solution under the visible-light irradiation



photogenerated electrons on the Ag conduction band can also be transferred to the conductive network system on the C-PDA, thereby suppressing the combination of photogenerated electrons and holes. Therefore, the addition of PDA obviously enhanced the photocatalytic properties of fabrics. In addition, the introduction of Ag nanoparticles can absorb visible light through the SPR effect and produce the separation of electrons and holes. When WO₃ was loaded onto the C-PDA-Ag composite photocatalytic fabric, a metal semiconductor Schottky barrier was rapidly formed. At this time, the C-PDA-Ag-WO₃(c) composite photocatalytic fabric was induced by the collective oscillation of the surface electrons of Ag, which enhanced the local internal electromagnetic field. The photogenerated electrons produced by the Ag nanoparticles had enough energy in a specific region (1.0–4.0 eV) to be irradiated by visible light, which was sufficient to overcome the Schottky barrier, thereby providing intrinsic power for visible light photocatalysis in the composite structure. Since the Ag nanoparticles were in direct contact with the crystalline WO₃ particles, the electrons would migrate from the conduction band of Ag to the conduction band of WO₃. At this time, the surface of WO₃ accumulated an excessive amount of e⁻, and the surface of Ag exhibited an excessive h⁺ (Yang et al. 2017b). The e⁻ on the surface of WO₃ were then

rapidly combined with O₂, resulting in a superoxide radical anion (·O₂⁻). Meanwhile, the residual h⁺ on Ag and WO₃ nanoparticles can oxidize hydroxide ions (OH⁻) to superoxide radicals (·OH) during the SPR process, which leads to low recombination of photogenerated electron–hole pairs (Adhikari et al. 2013). More importantly, the VB holes of WO₃ can also maintain direct oxidation of organic substances or oxidize OH⁻ to form ·OH. Therefore, it can be concluded that the degradation of organic pollutants seems to be associated with ·OH, ·O₂⁻ and h⁺ in the current research.

Conclusions

In summary, a novel visible light-responsive flexible C-PDA-Ag-WO₃(c) composite photocatalytic fabric was fabricated by a simple green synthetic route, in which a mild controllable chemical self-polymerization and reduction techniques were employed to fabricate uniform cubic Ag nanocrystals and UV irradiation and oxidation process were used to prepare WO₃ nanoparticles. The as-prepared photocatalytic flexible fiber had excellent photocatalytic performance and it can rapidly degrade RB-19 dye solution under visible light irradiation (degradation efficiency up to 98% in 180 min). The uniform deposition of Ag

and WO_3 layers on cotton fibers was confirmed by XRD, FE-SEM, EDS-mapping and XPS analysis. The results of photoelectrochemical measurement indicated that the doping of Ag and WO_3 was beneficial to prevent the recombination of photogenerated electron-hole pairs, and accelerated the effective separation of photogenerated electrons-holes and interface charge transfer. In addition, the C-PDA-Ag- WO_3 (c) composite photocatalytic fabric also exhibited excellent stability and reusability. The photocatalytic degradation mechanism of RB-19 on C-PDA-Ag- WO_3 (c) composite photocatalytic fabrics has been verified by experiments. This research may provide some new insights into the study of visible light responsive flexible fiber materials with nanostructures and it will have potential applications in photocatalysis and solar energy conversion fields.

Acknowledgments This research was supported by the Public Welfare Technology Application Research Project of Zhejiang Province China (LGG18E030002), the Natural Science Foundation of Shanghai (17ZR1400400) and Guangxi Innovation Drive Development Fund (AA17204076).

References

- Adhikari R, Gyawali G, Sekino T, Lee SW (2013) Microwave assisted hydrothermal synthesis of Ag/AgCl/ WO_3 photocatalyst and its photocatalytic activity under simulated solar light. *J Solid State Chem* 197:560–565
- Al-Ghafri B, Bora T, Sathe P, Dobrestov S, Al-Abri M (2018) Photocatalytic microbial removal and degradation of organic contaminants of water using PES fibers. *Appl Catal B* 233:136–142
- Antoniadou M, Daskalaki VM, Balis N, Kondarides DI, Korolis C, Lianos P (2011) Photocatalysis and photoelectrocatalysis using (CdS-ZnS)/ TiO_2 combined photocatalysts. *Appl Catal B* 107:188–196
- Boydjiev SI et al (2017) TiO_2/ZnO and ZnO/TiO_2 core/shell nanofibers prepared by electrospinning and atomic layer deposition for photocatalysis and gas sensing. *Appl Surf Sci* 424:190–197
- Bu Y, Chen Z, Sun C (2015) Highly efficient Z-scheme $\text{Ag}_3\text{PO}_4/\text{Ag}/\text{WO}_{3-x}$ photocatalyst for its enhanced photocatalytic performance. *Appl Catal B* 179:363–371
- Cao X et al (2018) A photochromic composite with enhanced carrier separation for the photocatalytic activation of benzylic C–H bonds in toluene. *Nat Catal* 1:704–710
- Chen J, Xio X, Wang Y, Ye Z (2019) Ag nanoparticles decorated $\text{WO}_3/g\text{-C}_3\text{N}_4$ 2D/2D heterostructure with enhanced photocatalytic activity for organic pollutants degradation. *Appl Surf Sci* 467:1000–1010
- Cheng W, He J, Dettelbach KE, Johnson NJJ, Sherbo RS, Berlinguette CP (2018) Photodeposited amorphous oxide films for electrochromic windows. *Chem* 4:821–832
- Ding J, Chai Y, Liu Q, Liu X, Ren J, Dai W-L (2016) Selective deposition of silver nanoparticles onto WO_3 nanorods with different facets: the correlation of facet-induced electron transport preference and photocatalytic activity. *J Phys Chem C* 120:4345–4353
- Ding J, Zhang L, Liu Q, Dai W-L, Guan G (2017) Synergistic effects of electronic structure of WO_3 nanorods with the dominant 001 exposed facets combined with silver size-dependent on the visible-light photocatalytic activity. *Appl Catal B* 203:335–342
- Ding K, Wang W, Yu D, Gao P, Liu B (2018) Facile formation of flexible Ag/AgCl/polydopamine/cotton fabric composite photocatalysts as an efficient visible-light photocatalysts. *Appl Surf Sci* 454:101–111
- Dong R, Tian B, Zeng C, Li T, Wang T, Zhang J (2013) Eco-friendly synthesis and photocatalytic activity of uniform cubic Ag@AgCl plasmonic photocatalyst. *J Phys Chem C* 117:213–220
- Dong Y-z, Xue Y-s, ang W-wY, SuY You H-m (2019) Visible light driven CdS/ WO_3 inverse opals with enhanced RhB degradation activity. *Colloids Surf A* 561:381–387
- Duan Y, Zhang M, Wang L, Wang F, Yang L, Li X, Wang C (2017) Plasmonic Ag- TiO_{2-x} nanocomposites for the photocatalytic removal of NO under visible light with high selectivity: the role of oxygen vacancies. *Appl Catal B* 204:67–77
- Elmaleh E, Saunders AE, Costi R, Salant A, Banin U (2008) Growth of photocatalytic CdSe-Pt nanorods and nanonets. *Adv Mater* 20:4312–4317
- Gao H, Sun Y, Zhou J, Xu R, Duan H (2013) Mussel-inspired synthesis of polydopamine-functionalized graphene hydrogel as reusable adsorbents for water purification. *ACS Appl Mater Interfaces* 5:425–432
- Gondal MA, Suliman MA, Dastageer MA, Chuah G-K, Basheer C, Yang D, Suwaiyan A (2016) Visible light photocatalytic degradation of herbicide (Atrazine) using surface plasmon resonance induced in mesoporous Ag- $\text{WO}_3/\text{SBA-15}$ composite. *J Mol Catal A Chem* 425:208–216
- Han S, Zhang X, Yu Q, Lei L (2012) Preparation of TiO_2/ITO film electrode by AP-MOCVD for photoelectrocatalytic application. *Sci China Chem* 55:2462–2470
- He C, Li X, Li Y, Li J, Xi G (2017) Large-scale synthesis of Au- WO_3 porous hollow spheres and their photocatalytic properties. *Catal Sci Technol* 7:3702–3706
- Higashi M, Domen K, Abe R (2011) Fabrication of efficient TaON and Ta_3N_5 photoanodes for water splitting under visible light irradiation. *Energy Environ Sci* 4:4138–4147
- Hu C, Peng T, Hu X, Nie Y, Zhou X, Qu J, He H (2010a) Plasmon-induced photodegradation of toxic pollutants with Ag-Agl/ Al_2O_3 under visible-light irradiation. *J Am Chem Soc* 132:857–862
- Hu L et al (2010b) Stretchable, porous, and conductive energy textiles. *Nano Lett* 10:708–714
- Hu X, Mu L, Wen J, Zhou Q (2012) Covalently synthesized graphene oxide-aptamer nanosheets for efficient visible-light photocatalysis of nucleic acids and proteins of viruses. *Carbon* 50:2772–2781

- Hu H, Chang M, Wang X, Chen D (2017) Cotton fabric-based facile solar photocatalytic purification of simulated real dye wastes. *J Mater Sci* 52:9922–9930
- Hu T, Li P, Zhang J, Liang C, Dai K (2018) Highly efficient direct Z-scheme WO_3/CdS -diethylenetriamine photocatalyst and its enhanced photocatalytic H_2 evolution under visible light irradiation. *Appl Surf Sci* 442:20–29
- Ji L W, Lin L, Yu D, Gao P, Wang W, Liu B J (2018) Solvent-free in situ synthesis of flexible $\text{BiVO}_4/\text{Bi}_2\text{WO}_6$: MWCNT, PET composites with superior mineralization potential for photocatalytic degradation of organic pollutants. *Mater Lett* 220:94–98
- Kim JH, Lee M, Park CB (2014) Polydopamine as a biomimetic electron gate for artificial photosynthesis. *Angew Chem Int Ed Engl* 53:6364–6368
- Li S, Zhang L, Wang H, Chen Z, Hu J, Xu K, Liu J (2014) Ta_3N_5 -Pt nonwoven cloth with hierarchical nanopores as efficient and easily recyclable macroscale photocatalysts. *Sci Rep* 4:3978
- Li Q, Duan G, Luo J, Liu X (2018) Ultrasonic-assisted synthesis of plasmonic Z-scheme $\text{Ag}/\text{AgCl}/\text{WO}_3$ -nanoflakes photocatalyst in geothermal water with enhanced visible-light photocatalytic performance. *J Energy Chem* 27:826–835
- Li Z et al (2019) Facile synthesis of WO_3 nanocuboids from tungsten trioxide powder and hydrogen peroxide. *Mater Lett* 236:197–200
- Liang Y, Lin S, Liu L, Hu J, Cui W (2015) Oil-in-water self-assembled $\text{Ag}@\text{AgCl}$ QDs sensitized Bi_2WO_6 : enhanced photocatalytic degradation under visible light irradiation. *Appl Catal B* 164:192–203
- Limmer SJ, Chou TP, Cao GZ (2004) A study on the growth of TiO_2 nanorods using sol electrophoresis. *J Mater Sci* 39:895–901
- Liu Y, Ai K, Lu L (2014) Polydopamine and its derivative materials: synthesis and promising applications in energy, environmental, and biomedical fields. *Chem Rev* 114:5057–5115
- Liu BJ, Lin L, Yu D, Sun J, Zhu ZJ, Gao P, Wang W (2018) Construction of fiber-based $\text{BiVO}_4/\text{SiO}_2/\text{reduced}$ graphene oxide (RGO) with efficient visible light photocatalytic activity. *Cellulose* 25:1089–1101
- Long Y, Wu J, Wang H, Zhang X, Zhao N, Xu J (2011) Rapid sintering of silver nanoparticles in an electrolyte solution at room temperature and its application to fabricate conductive silver films using polydopamine as adhesive layers. *J Mater Chem* 21:4875–4881
- Lv H, Liu Y, Tang H, Zhang P, Wang J (2017) Synergetic effect of MoS_2 and graphene as cocatalysts for enhanced photocatalytic activity of BiPO_4 nanoparticles. *Appl Surf Sci* 425:100–106
- Ma X, Jiang D, Xiao P, Jin Y, Meng S, Chen M (2017) 2D/2D heterojunctions of WO_3 nanosheet/ $\text{K}^+\text{Ca}_2\text{Nb}_3\text{O}_{10}^-$ ultrathin nanosheet with improved charge separation efficiency for significantly boosting photocatalysis. *Catal Sci Technol* 7:3481–3491
- Maeda K (2011) Photocatalytic water splitting using semiconductor particles: history and recent developments. *J Photochem Photobiol C* 12:237–268
- Meng Z et al (2015) Morphological and crystal structural control of tungsten trioxide for highly sensitive NO_2 gas sensors. *J Mater Chem C* 3:1134–1141
- Momeni MM, Ghayeb Y (2015) Visible light-driven photoelectrochemical water splitting on $\text{ZnO}-\text{TiO}_2$ heterogeneous nanotube photoanodes. *J Appl Electrochem* 45:557–566
- Momeni MM, Ghayeb Y, Davarzadeh M (2015) Single-step electrochemical anodization for synthesis of hierarchical WO_3-TiO_2 nanotube arrays on titanium foil as a good photoanode for water splitting with visible light. *J Electroanal Chem* 739:149–155
- Naik AJT, Warwick MEA, Moniz SJA, Blackman CS, Parkin IP, Binions R (2013) Nanostructured tungsten oxide gas sensors prepared by electric field assisted aerosol assisted chemical vapour deposition. *J Mater Chem A* 1:1827–1833
- Pan C, Liu X, Gong K, Mumtaz F, Wang Y (2018) Dopamine assisted PMOXA/PAA brushes for their switchable protein adsorption/desorption. *J Mater Chem B* 6:556–567
- Panayotov DA, Frenkel AI, Morris JR (2017) Catalysis and photocatalysis by nanoscale Au/TiO_2 : perspectives for renewable energy. *ACS Energy Lett* 2:1223–1231
- Paz EC et al (2018) Evaluation of H_2O_2 electrogeneration and decolorization of Orange II azo dye using tungsten oxide nanoparticle-modified carbon. *Appl Catal B* 232:436–445
- Ramstedt M, Franklyn P (2010) Difficulties in determining valence for Ag^0 nanoparticles using XPS-characterization of nanoparticles inside poly (3-sulphopropyl methacrylate) brushes. *Surf Interface Anal* 42:855–858
- Schlaich C et al (2018) Mussel-inspired polymer-based universal spray coating for surface modification: fast fabrication of antibacterial and superhydrophobic surface coatings. *Adv Mater Interfaces* 5:1701254
- Shi W, Zhang X, Brilllet J, Huang D, Li M, Wang M, Shen Y (2016) Significant enhancement of the photoelectrochemical activity of WO_3 nanoflakes by carbon quantum dots decoration. *Carbon* 105:387–393
- Shirke YM, Mukherjee SP (2017) Selective synthesis of WO_3 and $\text{W}_{18}\text{O}_{49}$ nanostructures: ligand-free pH-dependent morphology-controlled self-assembly of hierarchical architectures from 1D nanostructure and sunlight-driven photocatalytic degradation. *CrystEngComm* 19:2096–2105
- Shuang S, Lv R, Cui X, Xie Z, Zheng J, Zhang Z (2018) Efficient photocatalysis with graphene oxide/ $\text{Ag}/\text{Ag}_2\text{S}-\text{TiO}_2$ nanocomposites under visible light irradiation. *RSC Adv* 8:5784–5791
- Sun S, Wang W, Zeng S, Shang M, Zhang L (2010) Preparation of ordered mesoporous Ag/WO_3 and its highly efficient degradation of acetaldehyde under visible-light irradiation. *J Hazard Mater* 178:427–433
- Sun J et al (2017) Synthesis of Sb doping hierarchical WO_3 microspheres and mechanism of enhancing sensing properties to NO_2 . *J Alloys Compd* 692:876–884
- Tauc J (1966) Optical properties and electronic structure of amorphous Ge and Si. *Phys Status Solidi* 3:37–46
- Tian Y, Zhao Y, Gong C, Chai Y (2012) Effect of doping transition metal ions on photocatalysis of TiO_2 nanowires. *Appl Mech Mater* 217–219:203–206
- Vallejos S et al (2011) Au nanoparticle-functionalised WO_3 nanoneedles and their application in high sensitivity gas sensor devices. *Chem Commun* 47:565–567
- Varma RS, Thorat N, Fernandes R, Kothari DC, Patel N, Miotello A (2016) Dependence of photocatalysis on charge

- carrier separation in Ag-doped and decorated TiO₂ nanocomposites. *Catal Sci Technol* 6:8428–8440
- Wang C, Shao C, Wang L, Zhang L, Li X, Liu Y (2009) Electrospinning preparation, characterization and photocatalytic properties of Bi₂O₃ nanofibers. *J Colloid Interface Sci* 333:242–248
- Wang W, Li R, Tian M, Liu L, Zou H, Zhao X, Zhang L (2013) Surface silverized meta-aramid fibers prepared by bio-inspired poly(dopamine) functionalization. *ACS Appl Mater Interfaces* 5:2062–2069
- Wang Z, Hu M, Wei Y, Liu J, Qin Y (2016) Low-temperature NO₂-sensing properties and morphology-controllable solvothermal synthesis of tungsten oxide nanosheets/nanorods. *Appl Surf Sci* 362:525–531
- Wang P, Lu N, Su Y, Liu N, Yu H, Li J, Wu Y (2017a) Fabrication of WO₃@g-C₃N₄ with core@shell nanostructure for enhanced photocatalytic degradation activity under visible light. *Appl Surf Sci* 423:197–204
- Wang Y et al (2017b) Simultaneous synthesis of WO_{3-x} quantum dots and bundle-like nanowires using a one-pot template-free solvothermal strategy and their versatile applications. *Small* 13:1603689
- Wang X, Lu W, Chen Y, Li N, Zhu Z, Wang G, Chen W (2018a) Effective elimination of antibiotics over hot-melt adhesive sheath-core polyester fiber supported graphitic carbon nitride under solar irradiation. *Chem Eng J* 335:82–93
- Wang W, Lin L, Yu D, Baojiang Liu (2018b) Study on the photocatalytic performance of BiVO₄/Bi₂WO₆/multi-walled carbon nanotube nanocomposites in one-pot hydrothermal process. *J nanosci Nanotechnol* 11:7691–7702
- Wenderich K, Mul G (2016) Methods, mechanism, and applications of photodeposition in photocatalysis: a review. *Chem Rev* 116:14587–14619
- Xie R, Zhang L, Xu H, Zhong Y, Sui X, Mao Z (2015) Fabrication of Z-scheme photocatalyst Ag–AgBr@Bi₂₀TiO₃₂ and its visible-light photocatalytic activity for the degradation of isoproturon herbicide. *J Mol Catal A Chem* 406:194–203
- Xu H, Shi X, Ma H, Lv Y, Zhang L, Mao Z (2011) The preparation and antibacterial effects of dopa-cotton/AgNPs. *Appl Surf Sci* 257:6799–6803
- Yang S-F, Niu C-G, Huang D-W, Zhang H, Lianga C, Zeng G-M (2017) SrTiO₃ nanocubes decorated with Ag/AgCl nanoparticles as photocatalysts with enhanced visible-light photocatalytic activity towards the degradation of dyes, phenol and bisphenol A. *Environ Sci Nano* 4:585–595
- Yin X-B, Liu D-Y (2008) Polydopamine-based permanent coating capillary electrochromatography for auxin determination. *J Chromatogr A* 1212:130–136
- Yu J, Xiang Q, Zhou M (2009) Preparation, characterization and visible-light-driven photocatalytic activity of Fe-doped titania nanorods and first-principles study for electronic structures. *Appl Catal B* 90:595–602
- Yu W, Chen J, Shang T, Chen L, Gu L, Peng T (2017) Direct Z-scheme g-C₃N₄/WO₃ photocatalyst with atomically defined junction for H₂ production. *Appl Catal B* 219:693–704
- Zhang Z, Zhang J, Zhang B, Tang J (2013) Mussel-inspired functionalization of graphene for synthesizing Ag-polydopamine-graphene nanosheets as antibacterial materials. *Nanoscale* 5:118–123
- Zhang J, Liu Z, Liu Z (2016a) Novel WO₃/Sb₂S₃ heterojunction photocatalyst based on WO₃ of different morphologies for enhanced efficiency in photoelectrochemical water splitting. *ACS Appl Mater Interfaces* 8:9684–9691
- Zhang J, Zhang L, Shen X, Xu P, Liu J (2016b) Synthesis of BiOBr/WO₃ p–n heterojunctions with enhanced visible light photocatalytic activity. *CrystEngComm* 18:3856–3865
- Zhang M et al (2017a) In situ reduction of silver nanoparticles on hybrid polydopamine-copper phosphate nanoflowers with enhanced antimicrobial activity. *J Mater Chem B* 5:5311–5317
- Zhang Q, Dong R, Wu Y, Gao W, He Z, Ren B (2017b) Light-driven Au-WO₃@C janus micromotors for rapid photodegradation of dye pollutants. *ACS Appl Mater Interfaces* 9:4674–4683
- Zhang S et al (2017c) Unexpected ultrafast and high adsorption capacity of oxygen vacancy-rich WO_x/C nanowire networks for aqueous Pb²⁺ and methylene blue removal. *J Mater Chem A* 5:15913–15922
- Zhang J, Fu X, Hao H, Gan W (2018) Facile synthesis 3D flower-like Ag@WO₃ nanostructures and applications in solar-light photocatalysis. *J Alloys Compd* 757:134–141
- Zhao Y, Eley C, Hu J, Foord JS, Ye L, He H, Tsang SCE (2012) Shape-dependent acidity and photocatalytic activity of Nb₂O₅ nanocrystals with an active TT (001) surface. *Angew Chem Int Ed* 51:3846–3849
- Zhao H et al (2015) Fe₂O₃-AgBr nonwoven cloth with hierarchical nanostructures as efficient and easily recyclable macroscale photocatalysts. *RSC Adv* 5:10951–10959
- Zhou H, Wen Z, Liu J, Ke J, Duan X, Wang S (2019) Z-scheme plasmonic Ag decorated WO₃/Bi₂WO₆ hybrids for enhanced photocatalytic abatement of chlorinated-VOCs under solar light irradiation. *Appl Catal B* 242:76–84
- Zhu Z J, Han Q, Yu D, Sun J, Liu BJ (2017) A novel p-n heterojunction of BiVO₄/TiO₂/GO composite for enhanced visible-light-driven photocatalytic activity. *Mater Lett* 209:379–383
- Zhu Z J, Li Y, Wang C M, Liang L J, Yu D, Sun J, Gao P, Liu B J (2018) Facile synthesis and characterization of Bi₂MoO₆/Ag₃PO₄/RGO composites with enhanced visible-light-driven photocatalytic activity. *Mater Lett* 227:296–300

Publisher's Note Springer Nature remains neutral with regard to jurisdictional claims in published maps and institutional affiliations.